Computers and Fluids 166 (2018) 243–252

Contents lists available at ScienceDirect

Computers and Fluids

journal homepage: www.elsevier.com/locate/compfluid

An efficient high-order finite difference gas-kinetic scheme for the Euler and Navier–Stokes equations

Li-Jun Xuan[a,*], Kun Xu[b]

[a] Department of Aerospace Engineering, Auburn University, Auburn, AL 36849, United States
[b] Mathematics Department, Hong Kong University of Science and Technology, Clear Water Bay, Kowloon, Hong Kong

ARTICLE INFO

Article history:
Received 20 April 2017
Revised 16 October 2017
Accepted 23 January 2018

Keywords:
High-order
Finite-difference
Gas-kinetic scheme
WENO reconstruction

ABSTRACT

Based on the temporal evolution of the Navier-Stokes gas distribution function and Weighted Essential Non-Oscillatory (WENO) interpolation, a high-order finite difference gas-kinetic scheme (FDGKS) is constructed. Different from the previous high-order finite volume gas-kinetic method [Li, Xu, and Fu, J. Comput. Phys. vol. 229, pp. 6715 (2010)], which uses a discontinuous initial reconstruction at the cell interface, the present scheme is a finite-difference one with a continuous flow distribution at the grid point.

The time-accurate solution of the gas distribution function permits the FDGKS to be a one-step high-order scheme without multi-step Runge-Kutta temporal matching, which significantly reduces the computational time. Many numerical tests in solving one and two-dimensional Euler and Navier-Stokes equations demonstrate that FDGKS is a highly stable, accurate, and efficient scheme, which captures discontinuities without oscillations.

1. Introduction

The gas-kinetic schemes (GKS) have been well developed for compressible flow simulations, see [7,10,11,16–18] and references therein. The classical GKS uses the kinetic equation to model the dynamic processes around a cell interface [16]. Due to the discontinuous initial condition, the kinetic gas evolution covers the gas evolution process from the particle free transport in the kinetic scale to the Navier-Stokes solution construction in the hydrodynamic scale. The flow physics to be described in the evolution process depends on the ratio of the time step Δt to the particle collision time τ. While in 2013, based on a continuous initial condition around a cell interface, a new finite volume gas-kinetic scheme has been developed [19], which significantly reduces the computational cost. In smooth flow region, this type of construction is reasonable and the scheme provides an accurate Navier-Stokes solution. For the flow with discontinuous structure, the numerical dissipation needed to suppress the oscillation near a discontinuity in this scheme is implicitly imposed by the initial reconstruction, such as the use of the Weighted Essential Non-Oscillatory reconstruction (WENO) for characteristic variables. After initial data reconstruction, an analytic solution of the kinetic Bhatnagar–Gross–Krook (BGK) model [19] is used for the flux evaluation. In this work, we will further simplify the above finite volume procedure and construct a finite difference GKS.

In this paper, based on the time-accurate gas distribution function of the Navier–Stokes solution, a high order finite difference gas-kinetic scheme (FDGKS) is developed. Here a continuous flow distribution assumed at every grid point is used to evaluate the time-dependent flux function by solving the time-accurate gas distribution function, from which the numerical flux at the half grid point is reconstructed to update the grid variables in a conservative form. Like the high order finite difference scheme (FD) of Liu and Osher [8] and Jiang and Shu [6], in order to capture the discontinuity, the WENO procedure is employed in the reconstruction of the numerical flux.

The current FDGKS is in some sense quite similar to the finite difference WENO scheme with Lax-Wendroff type time discretization by Qiu and Shu [12], where a local solution is used to make the high-order time matching. Both of them are one-step schemes. But the FDGKS employs the local solution of the BGK equation, not the macroscopic one. It is very easy to obtain the local solution of the Navier–Stokes equation by solving the BGK equation. While for Lax-Wendroff type time discretization, a local solution for the Navier–Stokes equation is far more complex. There is no results in Qiu and Shu's paper [12] on the solving of the Navier–Stokes equation. But in this paper, the FDGKS would treat both Euler and Navier–Stokes equations.

* Corresponding author.
E-mail addresses: lzx0016@auburn.edu (L.-J. Xuan), makxu@ust.hk (K. Xu).

https://doi.org/10.1016/j.compfluid.2018.01.026
0045-7930/

The three novelties contributed in this paper includes

(1) The flux evaluation is based on a continuous initial distribution. Except for the work by Xuan and Xu [19], almost all of the other previous BGK methods solved the problem with the local discontinuous initial flow distribution. The continuous initial condition only needs one state flow variables. While the discontinuous initial condition relies on two states flow variables, which doubles the amount of CPU cost compared to the continuous treatment.
(2) The time-accurate Navier–Stokes gas distribution function (see Eq. (2)) has been used directly to calculate the evolution of the macroscopic flux function. The previous BGK solver depended on the integral-form solution as shown in [16]:

$$f(x,t,u,\xi) = \frac{1}{\tau}\int_{t^0}^{t} g(x-u(t-t'),t',u,\xi)e^{-(t-t')/\tau}\,\mathrm{d}t' + e^{-(t-t_0)/\tau} f_0(x-u(t-t_0),t_0,u,\xi),$$

where f_0 is the real gas distribution function f at time t_0, and g is the equilibrium state distribution function in space and time (x, t). The integral-form solution is far more complex and hence more costly than the one used in this paper.

Many one and two dimensional benchmark test cases are used to validate the accuracy and efficiency of the current FDGSK scheme. Numerical experiments show that FDGKS is a highly stable and efficient method, which provides a high resolution and has excellent performance in capturing a discontinuous solution. The extensive numerical verification shows that the FDGKS has the following distinguishable features:

(1) Due to the adoption of a continuous initial condition and the direct use of the time-accurate Navier-Stokes gas distribution function, the FDGKS is a highly efficient method. The FDGKS is essentially faster than the FD with the same WENO reconstruction and the same order time-matching.
(2) The FDGKS leads to slightly better resolution in all of the test cases than that of macroscopic equation based FD method [6] when same WENO reconstruction is used.
(3) The structure of the FDGKS is very similar to that of the FD. It is straightforward to modify any other FD code to the FDGKS by changing the computation of the point-wise flux.

In this paper, Section 2 presents the construction of the FDGKS in detail. The fifth-order WENO interpolation is introduced in Section 3. Section 4 encompasses the solution of many one and two dimensional benchmark flow problems by FDGKS, where the results are compared carefully with the ones obtained by the fifth-order finite-difference WENO method. The last section concludes this work.

2. Finite difference gas-kinetic scheme

In FDGKS, the distribution function at every grid point is firstly evaluated to obtain the pointwise time-averaged flux, then this flux is used to reconstruct the numerical flux at the half grid point, from which a conservative finite difference scheme can be constructed. In this section, we present the distribution function evaluation at the grid point using a gas-kinetic formulation leading to the construction of FDGKS.

2.1. One-dimensional flux evaluation at a grid point

On a uniform mesh with grid size Δx, at a grid point i, the macroscopic flow conservative variables are W_i and their derivatives can be approximated to 4th-order as

$$W_{i,x} = \left[\tfrac{2}{3}(W_{i+1}-W_{i-1}) + \tfrac{1}{12}(W_{i-2}-W_{i+2})\right]/\Delta x,$$
$$W_{i,xx} = \left[\tfrac{4}{3}(W_{i+1}+W_{i-1}) - \tfrac{1}{12}(W_{i-2}+W_{i+2}) - \tfrac{5}{2}W_i\right]/\Delta x^2. \quad (1)$$

At the grid point, it is not necessary to use WENO interpolation in calculating the above derivatives. To capture discontinuity only the construction of the numerical flux needs to be limited. (Similar conclusion has been realized previously in [12].) Then the time evolution of the distribution function from such an initial condition may be calculated as follow.

Based on the kinetic Bhatnagar–Gross–Krook (BGK) model [1], the corresponding Navier–Stokes (NS) distribution function $f(x, t, u, \xi)$ can be witten as

$$f(x,t,u,\xi) = g(x,t,u,\xi) - \tau Dg(x,t,u,\xi), \quad (2)$$

where g is the equilibrium state, u is the particle velocity, $\xi = (\xi_1, \xi_2, \cdots, \xi_K)$ is the internal variable, τ is the particle collision time, x and t are the spatial and temporal coordinates, and the operator $D \equiv \partial_t + u\partial_x$ ($\partial_\alpha \equiv \frac{\partial}{\partial \alpha}$). It should be noted that, for a diatomic gas with $\gamma = 1.4$, the total number of internal degrees of freedom K is 4 in onedimension and 3 in twodimensions, see [16,17]. Here for Navier–Stokes equation the collision time is determined by the shear viscosity coefficient μ and pressure p in the form of $\tau = \mu/p$ [16,17].

At the mesh grid point $\tilde{x}_i$, we assume the equilibrium state distribution function at this point to be g^e, a Maxwell-Boltzmann distribution corresponding to the equilibrium macroscopic flow state $W^e = [\rho^e, \rho^e U^e, E^e]^T$ can be written as

$$g^e = \rho^e \frac{\lambda}{2\pi} e^{-\lambda[(u-U^e)^2+\xi^2]}, \quad (3)$$

where ρ^e and U^e are the density and velocity, and λ is a function of temperature T^e, molecule mass m and Boltzmann constant k, with the relation $\lambda = \frac{m}{2kT^e}$. A 3rd-order Taylor expansion of the equilibrium state $g(x, t, u, \xi)$ near point $\tilde{x}_i$ may be expressed as

$$\begin{aligned} g &= g^e\left\{1 + a_x x + a_t t + \tfrac{1}{2}[(a_x^2 + a_{xx})x^2 + (a_t^2 + a_{tt})t^2] + (a_x a_t + a_{xt})xt\right\} \quad (4)\\ &= g^e\left[1 + a_x x + a_t t + \tfrac{1}{2}(A_{xx}x^2 + A_{tt}t^2) + A_{xt}xt\right], \end{aligned}$$

where $x = \tilde{x} - \tilde{x}_i$

$$A_{xx} = a_x^2 + a_{xx}, A_{tt} = a_t^2 + a_{tt}, A_{xt} = a_x a_t + a_{xt}; \quad (5)$$

$$a_x = a_{x,k}\psi_k,\ a_t = a_{t,k}\psi_k,\ a_{xx} = a_{xx,k}\psi_k, a_{xt} = a_{xt,k}\psi_k,\ a_{tt} = a_{tt,k}\psi_k, \quad (6)$$

with $\psi = [1, u, \frac{1}{2}(u^2+\xi^2)]^T, \xi^2 = \xi_1^2 + \ldots + \xi_K^2$ (K is the total number of internal degrees of freedom), and the repeated index k means summation of k from 1 to 3. $a_{x,k}$, $a_{t,k}$, $a_{xx,k}$, $a_{xt,k}$, $a_{tt,k}$ are coefficients to be determined. Then the Navier-Stokes distribution function $f(x, t, u, \xi)$ becomes

$$f = g^e\left\{\begin{array}{l} 1 + a_x x + a_t t + \frac{1}{2}(A_{xx}x^2 + A_{tt}t^2) + A_{xt}xt \\ -\tau[u(a_x + A_{xx}x + A_{xt}t) + a_t + A_{xt}x + A_{tt}t]\end{array}\right\}. \quad (7)$$

We can calculate the coefficients of spatial derivatives in the distribution functions $\{a_{x,k}, a_{xx,k}\}_{k=1,2,3}$ from the derivatives of macroscopic conservative flow variables W_α ($\alpha = 1, 2, 3$) at the grid point i (see [9])

$$\langle a_x\rangle = \frac{\partial W_\alpha}{\partial x}, \quad \langle A_{xx}\rangle = \frac{\partial^2 W_\alpha}{\partial x^2}; \quad \langle\bullet\rangle \equiv \int \bullet g^e \psi_\alpha\,\mathrm{d}\Xi, \quad (8)$$

where $\mathrm{d}\Xi = \mathrm{d}u\,\mathrm{d}\xi$ is the volume element in the phase space and $\mathrm{d}\xi = \mathrm{d}\xi_1\,\mathrm{d}\xi_2 \ldots \mathrm{d}\xi_K$, g^e is the Maxwellian distribution corresponding to W_α. As an illustration, the procedures to solve a_x and $a_{xx} = A_{xx} - a_x^2$ are:

(1). Solve $a_{x,k}$ by expanding the equation $\langle a_x\rangle = \partial_x W_\alpha$ as

$$\int a_{x,k}\psi_k\psi_\alpha g^e \,\mathrm{d}\Xi = \partial_x W_\alpha. \tag{9}$$

In this linear system the calculation of the coefficients matrix $\int \psi_k\psi_\alpha g^e \,\mathrm{d}\Xi$ eventually reduces to computing the moments of $\langle\langle u^n\rangle\rangle, \langle\langle \xi^{2n}\rangle\rangle (n = 0, 1, \cdots)$ (see [17]), which is defined as

$$\langle\langle u^n\rangle\rangle = \frac{1}{\rho^e}\int u^n g^e \,\mathrm{d}\Xi, \quad \langle\langle \xi^{2n}\rangle\rangle = \frac{1}{\rho^e}\int \xi^{2n} g^e \,\mathrm{d}\Xi. \tag{10}$$

From the Maxwellian distribution of g^e (3), it is easy to deduce that

$$\langle\langle u^0\rangle\rangle = 1, \quad \langle\langle u^1\rangle\rangle = U^e, \quad \langle\langle u^{k+2}\rangle\rangle = U^e\langle\langle u^{k+1}\rangle\rangle + \frac{k+1}{2\lambda}\langle\langle u^k\rangle\rangle;$$

and

$$\langle\langle \xi^2\rangle\rangle = \frac{K}{2\lambda}, \qquad \langle\langle \xi^4\rangle\rangle = \frac{3K}{4\lambda^2} + \frac{K(K+1)}{4\lambda^2}, \cdots$$

(2). Solve $a_{xx,k}$ by expanding $\langle A_{xx}\rangle = \partial_{xx}^2 W_\alpha$ to

$$\int a_{xx,k}\psi_k\psi_\alpha g^e \,\mathrm{d}\Xi = \partial_{xx}^2 W_\alpha - \int a_{x,j}\psi_j a_{x,j}a_{x,k}\psi_j a_{x,k}\psi_\alpha g^e \,\mathrm{d}\Xi. \tag{11}$$

It is also finally reduced to computing the moments of $\langle\langle u^n\rangle\rangle$, $\langle\langle \xi^{2n}\rangle\rangle$.

After the determination of $a_{x,k}$ and $a_{xx,k}$, based on the compatibility condition

$$\langle f - g\rangle = 0, \tag{12}$$

we have (see [9])

$$\langle ua_x + a_t\rangle = 0, \ \langle uA_{xx} + A_{xt}\rangle = 0, \ \langle uA_{xt} + A_{tt}\rangle = 0. \tag{13}$$

By definition of A_{xx}, A_{xt}, and A_{tt} in (5), Eq. (13) gives the solutions to coefficients $\{a_{t,k}, a_{xt,k}, a_{tt,k}\}_{k=1,2,3}$, follows the same procedures in solving a_x and a_{xx}.

After these algorithms, the one-dimension NS distribution function $f(x, t, u, \xi)$ is fully solved, and then the fluxes $F(t)$ for the macroscopic variables at x_i can be computed using

$$F(t) = \int uf\psi \,\mathrm{d}\Xi = F^c(t) - F^v(t), \tag{14}$$

where $F^v(t) = \tau\int uDg\psi \,\mathrm{d}\Xi$ is the viscous flux,

$$F^v(t) = \tau\big[\langle u^2 a_x\rangle + \langle ua_t\rangle + (\langle u^2 A_{xt}\rangle + \langle uA_{tt}\rangle)t\big], \tag{15}$$

and $F^c(t)$ is the Euler flux which can be calculated directly from the conservative variables $W(t)$ corresponding to $g(t)$, i.e.,

$$\begin{aligned} W(t) &= \int g\psi \,\mathrm{d}\Xi = W^e + \langle a_t\rangle t + \tfrac{1}{2}\langle A_{tt}\rangle t^2, \\ F^c(t) &= [\rho U, \rho U^2 + p, (E+p)U]^T, \end{aligned} \tag{16}$$

in which ρ, U, E, p represent the density, velocity, total energy, and pressure, which are determined by $W(t)$, and W^e is the conservative variable corresponding to g^e.

For the time interval $t \in [t^n, t^{n+1}]$, we define a time step $\Delta t = t^{n+1} - t^n$, to make the calculation of the time averaged flux $\bar{F}_i = \frac{1}{\Delta t}\int_{t^n}^{t^{n+1}} F(t)\,\mathrm{d}t$ accurate to 2nd-order polynomial tiwth respect to t (shown in (16)), we choose two Gauss–Legendre points (t_{G1}, t_{G2}) in $[0, \Delta t]$ and calculate the corresponding F^c and F^v, then use a 3rd-order Gauss quadrature to compute the time integral, we get

$$\bar{F}_i = \tfrac{1}{2}[F^c(t_{G1}) - F^v(t_{G1}) + F^c(t_{G2}) - F^v(t_{G2})]. \tag{17}$$

After the flux evaluation at the grid point, the classical conservative upwind finite difference method based on Lax–Friedrich flux splitting is used to update the grid point values in the following steps. To capture the discontinuity, 5th-order WENO reconstruction is used to calculate the numerical flux. The details will be shown in Section 3.

2.2. Two-dimensional gas-kinetic flux

For a rectangular mesh on grid point (x_i, y_j) $(i = 1, \ldots, N; j = 1, \ldots, M)$, the derivatives of the macroscopic conservative variables in x and y directions $(W_{i,j,x}, W_{i,j,y}, W_{i,j,xx}, W_{i,j,yy})$ are calculated in the same ways as in the one-dimension case. While the cross derivatives are calculated to 4th-order accuracy by

$$W^{(1)}_{i,j,xy} = (\tfrac{2}{3}(W_{i+1,j,y} - W_{i-1,j,y}) + \tfrac{1}{12}(W_{i-2,j,y} - W_{i+2,j,y}))/\Delta x, \tag{18}$$

$$W^{(2)}_{i,j,xy} = (\tfrac{2}{3}(W_{i,j+1,x} - W_{i,j-1,x}) + \tfrac{1}{12}(W_{i,j-2,x} - W_{i,j+2,x}))/\Delta y, \tag{19}$$

and $W_{i,j,xy} = \frac{1}{2}(W^{(1)}_{i,j,xy} + W^{(2)}_{i,j,xy})$.

At the grid point, a 3rd-order Taylor expansion of the equilibrium state is

$$\begin{aligned} g = g^e\big[&1 + a_x x + a_y y + a_t t + \tfrac{1}{2}(A_{xx}x^2 + A_{yy}y^2 + A_{tt}t^2) \\ &+ A_{xy}xy + A_{xt}xt + A_{yt}yt\big], \end{aligned} \tag{20}$$

with $A_{yy} = a_y^2 + a_{yy}, A_{xy} = a_x a_y + a_{xy}, A_{yt} = a_y a_t + a_{yt}$, $a_x = a_{x,k}\psi_k, \ldots$ $(k = 1, 2, 3, 4)$ and $\psi = [1, u, v, \frac{1}{2}(u^2 + v^2 + \xi^2)]$. Based on the NS distribution function $f = g - \tau Dg$, its expansion becomes

$$f = g^e\left\{\begin{array}{l} 1 + a_x x + a_y y + a_t t + \frac{1}{2}(A_{xx}x^2 + A_{yy}y^2 + A_{tt}t^2) \\ +A_{xy}xy + A_{xt}xt + A_{yt}yt - \tau[u(a_x + A_{xx}x + A_{xy}y + A_{xt}t) \\ +v(a_y + A_{xy}x + A_{yy}y + A_{yt}t) + a_t + A_{xt}x + A_{yt}y + A_{tt}t] \end{array}\right\}. \tag{21}$$

Again, the spatial derivatives in (21) are determined from

$$\begin{aligned} &\langle a_x\rangle = \partial_x W, \ \langle a_y\rangle = \partial_y W, \ \langle A_{xx}\rangle = \partial_{xx}W, \ \langle A_{xy}\rangle = \partial_{xy}W, \\ &\langle A_{yy}\rangle = \partial_{yy}W. \end{aligned} \tag{22}$$

We can further derive other derivatives from the compatibility condition (12) as

$$\begin{aligned} &\langle ua_x + va_y + a_t\rangle = 0, \ \langle uA_{xx} + vA_{xy} + A_{xt}\rangle = 0, \\ &\langle uA_{xy} + vA_{yy} + A_{yt}\rangle = 0, \ \langle uA_{xt} + vA_{yt} + A_{tt}\rangle = 0. \end{aligned} \tag{23}$$

After the determination of the distribution function $f(x, y, t, u, v, \xi)$, the convective and viscous fluxes at grid point (x_i, y_j) become

$$\begin{aligned} F^c(t) &= [\rho U, \rho U^2 + p, \rho UV, (E+p)U]^T, \\ F^v(t) &= \tau\int uDg\psi \,\mathrm{d}\Xi \\ &= \tau[\langle u^2 a_x + uva_y + ua_t\rangle + \langle u^2 A_{xt} + uvA_{yt} + uA_{tt}\rangle t], \end{aligned} \tag{24}$$

where the physical variables (ρ, U, V, E, p) are determined from the conservative variables $W(t)$ corresponding to g,

$$W(t) = \int g\psi \,\mathrm{d}\Xi = W^e + \langle a_t\rangle t + \tfrac{1}{2}\langle A_{tt}\rangle t^2, \tag{25}$$

W^e is the interpolated value at the grid point, which is used to determine g^e. The vertical fluxes are given by

$$\begin{aligned} G^c(t) &= [\rho V, \rho UV, \rho V^2 + p, (E+p)V]^T, \\ G^v(t) &= \tau\int vDg\psi \,\mathrm{d}\Xi \\ &= \tau[\langle uva_x + v^2 a_y + va_t\rangle + \langle uvA_{xt} + v^2 A_{yt} + vA_{tt}\rangle t]. \end{aligned} \tag{26}$$

It is well known that the BGK equation assumes a unit Prandtl number. The Prandtl number can be corrected through the modification of the heat-flux [17], using

$$\begin{aligned} q_x &= \frac{1}{2}\int (u-U)[(u-U)^2 + (v-V)^2 + \xi^2]f \,\mathrm{d}\Xi \\ &= UF_2^v + VF_3^v - F_4^v, \\ q_y &= \frac{1}{2}\int (v-V)[(u-U)^2 + (v-V)^2 + \xi^2]f \,\mathrm{d}\Xi \end{aligned}$$

$$= UG_2^v + VG_3^v - G_4^v. \quad (27)$$

The Prandtl number may be modified using a correction of the energy flux, namely

$$F_4^{Fix} = F_4^v + (1/Pr - 1)q_x, \quad G_4^{Fix} = G_4^v + (1/Pr - 1)q_y. \quad (28)$$

To get the time averaged flux $\bar{F} = \frac{1}{\Delta t}\int_{t^n}^{t^{n+1}} F(t)\,dt$ and $\bar{G} = \frac{1}{\Delta t}\int_{t^n}^{t^{n+1}} G(t)\,dt$, we choose two Gauss-Legendre points (t_{G1}, t_{G2}) in $[0, \Delta t]$ and calculate the corresponding F and G. The Gaussian quadrature can be used to compute the time integral to 3rd-order accuracy, thus leading to

$$\bar{F} = \tfrac{1}{2}[F(t_{G1}) + F(t_{G2})], \quad \bar{G} = \tfrac{1}{2}[G(t_{G1}) + G(t_{G2})]. \quad (29)$$

With this approach, both temporal averaged convective and viscous fluxes $(\bar{F}^c_{i,j}, \bar{F}^v_{i,j}, \bar{G}^c_{i,j}, \bar{G}^v_{i,j})$ are computed at every node point (i, j).

Subsequently the Lax–Friedrich flux splitting may be combined with a 5th-order WENO reconstruction to compute the convective numerical fluxes. As for the viscous numerical fluxes, they may be simply represented by central 6th-order interpolation, namely

$$\hat{F}^v_{i+1/2,j} = \frac{\bar{F}^v_{i+3,j} + \bar{F}^v_{i-2,j} - 8(\bar{F}^v_{i+2,j} + \bar{F}^v_{i-1,j}) + 37(\bar{F}^v_{i+1,j} + \bar{F}^v_{i,j})}{60},$$
$$\hat{G}^v_{i,j+1/2} = \frac{\bar{G}^v_{i,j+3} + \bar{G}^v_{i,j-2} - 8(\bar{G}^v_{i,j+2} + \bar{G}^v_{i,j-1}) + 37(\bar{G}^v_{i,j+1} + \bar{G}^v_{i,j})}{60}. \quad (30)$$

The total numerical flux may thus be deduced from $\hat{F}_{i+1/2,j} = \hat{F}^c_{i+1/2,j} - \hat{F}^v_{i+1/2,j}$, and $\hat{G}_{i,j+1/2} = \hat{G}^c_{i,j+1/2} - \hat{G}^v_{i,j+1/2}$.

Finally, the grid point values may be updated from

$$W^{n+1}_{ij} = W^n_{i,j} - \frac{\Delta t}{\Delta x}(\hat{F}_{i+1/2,j} - \hat{F}_{i-1/2,j}) - \frac{\Delta t}{\Delta y}(\hat{G}_{i,j+1/2} - \hat{G}_{i,j-1/2}). \quad (31)$$

Remark.

1. For a temporal second-order scheme, a first order Taylor expansion of the kinetic distribution function is sufficient. All 2nd-order derivatives in the temporal evolution of the kinetic distribution function can be ignored.
2. The Lax–Friedrich flux-splitting with 5th-order WENO reconstruction is used to calculate the convective numerical flux at half grid points, shown in the next section. The scheme constructed here has a 3rd-order convergence accuracy in time and 5th-order convergence accuracy in space. These are validated numerically in Section 4.

3. Fifth-order WENO interpolation for numerical fluxes at half grid point

With the physical fluxes at every grid point, a 5th-order WENO reconstruction may be used to compute the numerical flux at the half grid point, and thus capture the discontinuous solution without oscillation. Here Jiang and Shu's weight [6] is used.

(1) With the conservative variables W_i at grid point, at half a grid point $i + 1/2$, use the averaged value $W_{i+1/2} = \frac{1}{2}(W_i + W_{i+1})$ to calculate the left and right eigenvector matrix $L_{i+1/2}$ and $R_{i+1/2}$ and the eigenvalues $\lambda_\alpha(\alpha = 1, 2, 3)$.

(2) Project the conservative variables W_{i+l} $(l = -2, \cdots, 3)$ and time averaged kinetic flux $\bar{F}_{i+l}$ at grid points to characteristic ones $\tilde{W}_{i+l}$ and $\tilde{F}_{i+l}$ by

$$\tilde{W}_{i+l} = L_{i+1/2}W_{i+l}, \quad \tilde{F}_{i+l} = L_{i+1/2}\bar{F}_{i+l}. \quad (32)$$

(3) For αth component, make the flux splitting

$$F^{\pm}_{i+l,\alpha} = \tfrac{1}{2}(\tilde{F}_{i+l,\alpha} \pm c_\alpha \tilde{W}_{i+l,\alpha}), \quad (33)$$

where $c_\alpha = \max_l(|\lambda_{\alpha,i+l}|)$.

(4) Conduct WENO interpolation:

$$F^{(1)} = \tfrac{11}{6}F^+_i - \tfrac{7}{6}F^+_{i-1} + \tfrac{1}{3}F^+_{i-2},$$
$$F^{(2)} = \tfrac{5}{6}F^+_i - \tfrac{1}{6}F^+_{i-1} + \tfrac{1}{3}F^+_{i+1},$$
$$F^{(3)} = \tfrac{1}{3}F^+_i - \tfrac{1}{6}F^+_{i+2} + \tfrac{5}{6}F^+_{i+1}, \quad (34)$$

and

$$IS_1 = \tfrac{13}{12}(F^+_i + F^+_{i-2} - 2F^+_{i-1})^2 + \tfrac{1}{4}(3F^+_i + F^+_{i-2} - 4F^+_{i-1})^2,$$
$$IS_2 = \tfrac{13}{12}(F^+_{i+1} + F^+_{i-1} - 2F^+_i)^2 + \tfrac{1}{4}(F^+_{i+1} - F^+_{i-1})^2,$$
$$IS_3 = \tfrac{13}{12}(F^+_i + F^+_{i+2} - 2F^+_{i+1})^2 + \tfrac{1}{4}(3F^+_i + F^+_{i+2} - 4F^+_{i+1})^2,$$
$$d_1 = 0.1, \ d_2 = 0.6, \quad d_3 = 0.3. \quad (35)$$

The JS weight is

$$w_s = \beta_s / \sum_{p=1}^{3}\beta_p, \quad \beta_s = d_s/(IS_s^2 + \epsilon) \ (s = 1, 2, 3), \quad (36)$$

where $\epsilon = 10^{-6}$.

Then, the '+' splitting flux at half grid point becomes

$$\tilde{F}^+_{i+1/2} = \textstyle\sum_{p=1}^{3} w_p F^{(p)}. \quad (37)$$

Similar procedures are used to obtain the '−' splitting flux $\tilde{F}^-_{i+1/2}$ from F^-_{i+l}. And then

$$\tilde{F}_{i+1/2} = \tilde{F}^+_{i+1/2} + \tilde{F}^-_{i+1/2}, \quad \hat{F}_{i+1/2} = R_{i+1/2}\tilde{F}_{i+1/2}. \quad (38)$$

In two-dimensional case, the interpolation of numerical flux $\hat{G}_{i+1/2}$ can be obtained in the same way as in x-direction.

4. Numerical experiments

The performance of finite difference gas-kinetic scheme with 5th-order WENO interpolation (FDGKS-W5) will be tested in this section. Many one and two dimensional benchmark problems are calculated and the results and CPU time are compared with those of 5th-order WENO macroscopic equation based finite difference under the same flux splitting and WENO reconstruction (noted as FD-W5). A 3rd-order TVD Runge–Kutta method [6] is used in FD-W5 to make the time matching.

4.1. One dimensional cases

4.1.1. Stability test

The stability property is numerically tested for the Euler equations with initial condition

$$\rho = 1 + \tfrac{1}{4}\sin(\tfrac{2\pi}{5}x), \quad U = 1, \quad p = 1, \quad (39)$$

where ρ is density, U is velocity, and p is pressure. Periodic boundary conditions are set at both ends in the computational domain $x \in [-5, 5]$. For this case, the maximum stable CFL number is 1.31, which shows high stability of FDGSK-W5.

4.1.2. Accuracy test

To test the accuracy, the case (39) is used for the inviscid solution. The computation is run for one period of time $t = 10$. The L_1 and L_∞ errors of FGDKS-W5 are compared those of FD-W5 in Table 1, where N is the number of grid. We can see that FDGKS-W5 has well achieved the designed 5th-order with a slightly smaller error than that of FD-W5.

For the temporal accuracy, 320 grids have been used and the results of numerical experiments in Table 2 show that the designed 3rd-order has almost been achieved (Numbers in the parentheses after the time step are the corresponding CFL numbers). With the decrease of the time step, the error drops to the spatial error limited by spatial discretization on the finite grid size and hence the order is getting lower.

Table 1
One dimensional Euler equation; convection of density sine wave; periodic boundary conditions. Compare the error convergence of FD-W5 and FDGKS-W5.

	FD-W5				FDGKS-W5			
N	L_1 error	Order	L_∞ error	Order	L_1 error	Order	L_∞ error	Order
20	2.179e−2	–	3.540e−2	–	1.514e−2	–	2.332e−2	–
40	1.310e−3	4.06	2.083e−3	4.09	7.860e−4	4.27	1.572e−3	3.89
80	4.724e−5	4.79	8.855e−5	4.56	2.356e−5	5.06	5.663e−5	4.79
160	1.464e−6	5.01	3.315e−6	4.73	7.170e−7	5.38	1.741e−6	5.02
320	3.158e−8	5.53	6.676e−8	5.63	2.208e−8	5.21	5.490e−8	4.99

Table 2
The temporal error convergence of FDGKS-W5 on grid of $N = 320$.

Δt	1.192e−2(0.9)	1.060e−2(0.8)	9.274e−3(0.7)	7.949e−3(0.6)	6.624e−3(0.5)
L_1 error	2.924e−7	2.094e−7	1.448e−7	9.633e−8	6.160e−8
Order	–	2.84	2.76	2.64	2.45
L_∞ error	4.431e−7	3.124e−7	2.106e−7	1.373e−7	9.060e−8
Order	–	2.98	2.95	2.77	2.28

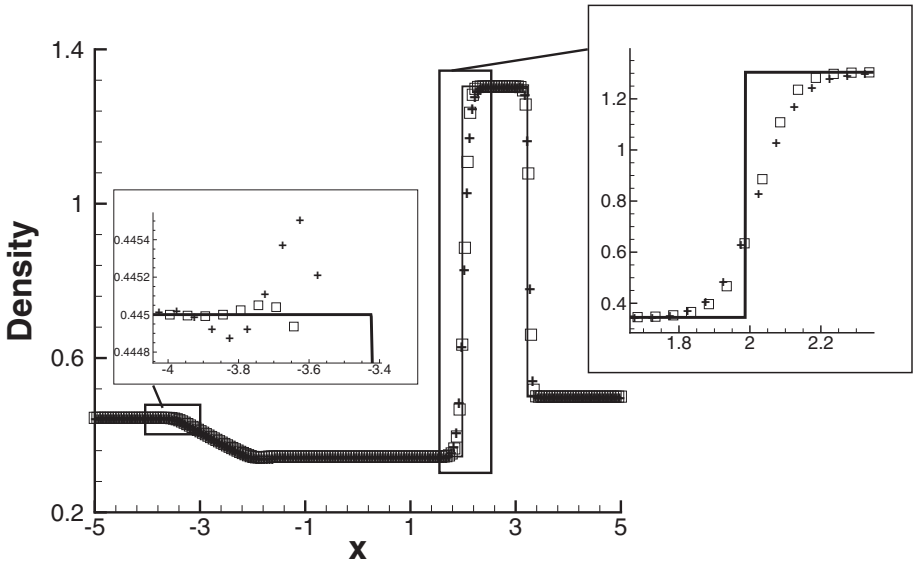

Fig. 1. Density profile for Lax problem with $N = 200$ grid points and CFL = 0.6. Solid line: exact solution; square: FDGKS-W5; '+': W5-JS.

4.1.3. Tests for discontinuous flows and efficiency of the schemes

Now we compare the results of FD-W5 and FDGKS-W5 for the flow simulations with shock and contact discontinuities. In all of the following test cases, to be consistent with Jiang-Shu's paper [6], the CFL number is set to be 0.6.

Example 4.1. Lax problem

This is a Riemann problem for the Euler solution with the initial condition:

$$\begin{aligned}&(\rho, U, p) = (0.445, 0.698, 3.528) \quad \text{for } x \in [-5, 0],\\ &(\rho, U, p) = (0.5, 0, 0.571) \quad \text{for } x \in (0, 5].\end{aligned} \tag{40}$$

The computation is run up to time $t = 1.3$. $N = 200$ grid points are used in the computational domain $x \in [-5, 5]$. Fig. 1 shows that both schemes obtain acceptable results. The zoomed in solution shows that FDGKS-W5 seems has smaller oscillation and higher resolution for discontinuity than those of FD-W5 for this case. Velocity and pressure distributions from FDGKS-W5 are shown in Fig. 2.

Example 4.2. Blast wave problem

This problem is from [15]. The computational domain has $x \in [-5, 5]$ with initial condition

$$\rho = 1; \quad U = 0; \quad p = \begin{cases} 1000, & x \in [-5, -4), \\ 0.01, & x \in [-4, 4), \\ 100, & x \in [4, 5]. \end{cases} \tag{41}$$

The output time is $t = 0.38$. The density profiles on meshes with $N = 200$ and $N = 400$ grid points by FD-W5 are FDGKS-W5 are presented in Fig. 3. The reference solution is obtained by FD-W5 on a mesh with $N = 10000$ grid points. The FDGKS-W5 has similar resolution as FD-W5 in this case.

Example 4.3. Shock acoustic-wave interaction

The shock acoustic-wave interaction problem is given in [13]. The computational domain is $x \in [-5, 5]$ with initial condition

$$(p, U, \rho) = \begin{cases} (3.857134, 2.629369, 10.33333), & x < -4, \\ (1 + 0.2\sin(5x), 0, 1), & x \geq -4. \end{cases} \tag{42}$$

The output time is $t = 1.8$. The reference solution is obtained by FD-W5 with $N = 10,000$ grid points. Fig. 4 shows that FDGKS-W5 achieves similar resolution as FD-W5.

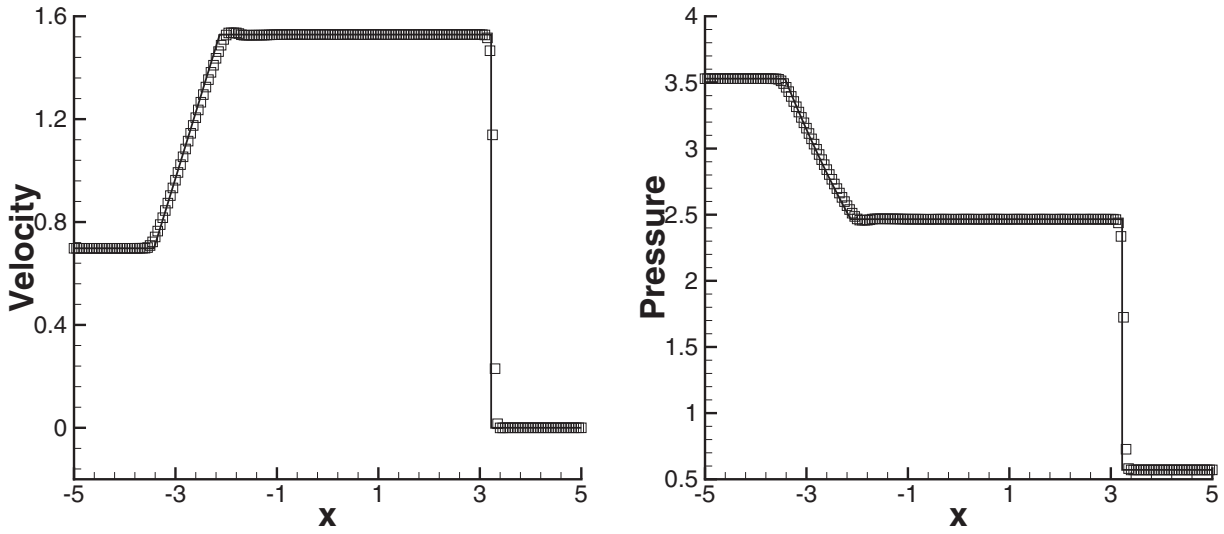

Fig. 2. Lax problem by FDGKS-W5 with $N = 200$ grid points and CFL = 0.6. Left: velocity, right: pressure. Solid line: exact solution; square: solution by FDGKS-W5.

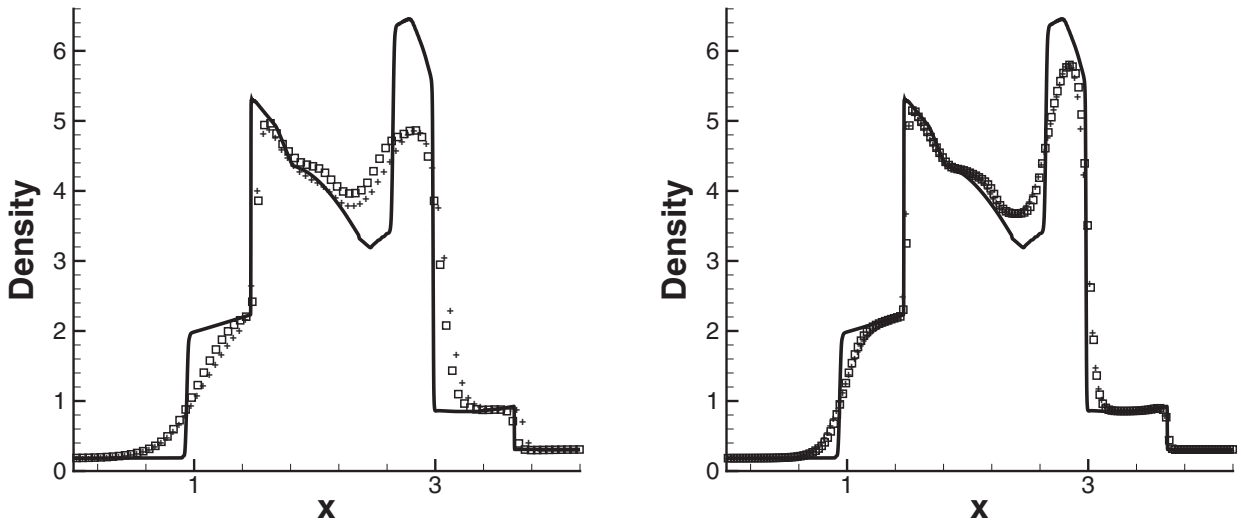

Fig. 3. Density profiles in blast wave problem. Thick solid line: reference solution (FD-W5 with $N = 10000$ grid points); □ : FDGKS-W5; '+': FD-W5. Left: $N = 200$; right: $N = 400$.

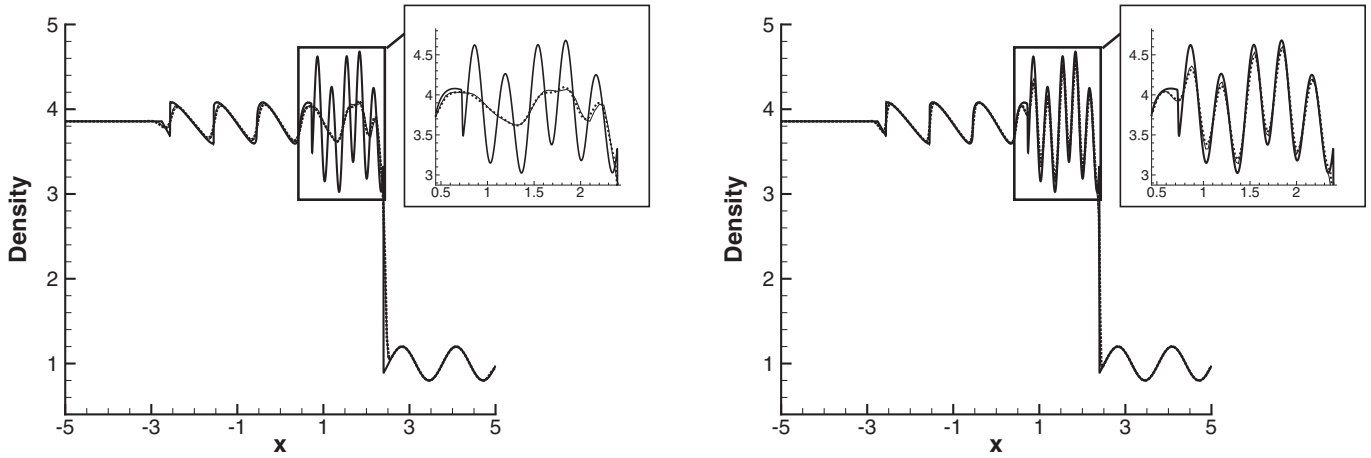

Fig. 4. Density profiles of Shu-Osher problem. CFL = 0.6. Thick solid line: reference solution (FD-W5 with $N = 10000$ grid points); thin solid line: FDGKS-W5, dotted line: FD-W5. Left: $N = 200$; right: $N = 400$.

Table 3
CPU times for different schemes and test cases.

	Lax Problem	Shu-Osher	Blast wave
FD-W5	133.27s	272.12s	500.02s
FDGKS-W5	57.06s	116.86s	214.59s
Speedup Ratio	2.335	2.328	2.330

Table 4
The error convergence of FDGKS-W5 for the 2-D convection of density wave problem.

$N_x \times N_y$	L_1 error	Order	L_∞ error	Order
8 × 12	2.028e−2	–	3.139e−2	–
16 × 24	1.396e−3	3.86	2.229e−3	3.82
32 × 48	5.429e−5	4.68	1.021e−4	4.45
64 × 96	1.605e−6	5.08	3.259e−6	4.97
128 × 192	3.479e−8	5.52	7.399e−8	5.46

4.1.4. Compuational cost

The above Examples 4.1–4.3 are used to test the efficiency of the schemes. In the test cases, a grid with $N = 10000$ points are used and the time step is given by CFL = 0.5. The CPU time costs are shown in Table 3, where the FDGKS-W5 is about 1.3 times faster than FD-W5. The FDGKS-W5 is a one-step scheme, where for each time step it only needs one time of WENO reconstruction and flux computation. But in FD-W5, because of the multi-step temporal update, we need 3 times of WENO reconstruction and flux calculation for every time step. This is the reason why FDGKS-W5 is more efficient than FD-W5.

4.2. Two dimensional cases

In this subsection, we are going to present the results of FDGKS-W5 in simulating two-dimensional cases and compare them with those of FD-W5.

4.2.1. Accuracy test

Example 4.4. Propagation of density sine wave [12] for Euler equation

For Euler equation, the initial density $\rho(x, y, 0) = 1 + 0.2\sin[\pi(x + y)]$, velocity $U(x, y, 0) = 0.7$, $V(x, y, 0) = 0.3$, and pressure $p(x, y, 0) = 1$; with periodic boundary conditions in both x- and y- directions. The exact solution is $\rho = 1 + 0.2\sin(\pi(x + y - (U + V)t))$, $U = 0.7$, $V = 0.3$, $p = 1$. The computation domain is $[0, 2] \times [0, 2]$. Uniform mesh is used in both x and y directions. To avoid any special error cancellation due to the symmetry axis being in the diagonals of cells, the mesh sizes in the x- and y-directions are different. Table 4 shows the errors of FDGKS-W5. Here we neglect the results of FD-W5, because they are almost the same as those of FDGKS-W5. We can see that FDGKS-W5 achieves the designed order.

Example 4.5. Convection of isotropic vortex for Navier–Stokes equation

This is convection of isotropic vortex in a two-dimensional domain. The problem is set up in a computational domain $(x, y) \in [0, 10] \times [0, 10]$. The periodic boundary condition is imposed in both x- and y- directions. The initial conditions are given by

$$\begin{aligned}
&(U(x, y, 0), V(x, y, 0)) = (1, 1) + \tfrac{\epsilon}{2\pi} e^{0.5(1-r^2)}(-\bar{y}, \bar{x}),\\
&T(x, y, 0) = 1 - \frac{(\gamma - 1)\epsilon^2}{8\gamma\pi^2} e^{1-r^2},\\
&S(x, y, 0) = 1, \quad \rho(x, y, 0) = 1,
\end{aligned} \tag{43}$$

where the temperature T and the entropy S are related to the density ρ and the pressure p by $T = p/\rho$, $S = p/\rho^\gamma$, and $(\bar{x}, \bar{y}) = (x - 5, y - 5)$, $r^2 = \bar{x}^2 + \bar{y}^2$, and the vortex strength $\epsilon = 5$. For inviscid flow, the exact solution is an isotropic vortex convected with the speed (1, 1) in the diagonal direction. While for viscous flow, the reference solution can only be obtained numerically. A 6th-order finite difference method is used to compute the reference solution on a mesh of 257×257. The vector L_1 and L_∞ errors are defined as

$$L_1 = \frac{1}{N^2}\sum_{i,j} |\rho_{i,j} - \rho^r_{i,j}|, \quad L_\infty = \max_{i,j} |\rho_{i,j} - \rho^r_{i,j}|, \tag{44}$$

where $\rho_{i,j}$ is the density on the node (i, j) and $\rho^r_{i,j}$ is the corresponding reference solution; N is the number of point on x direction, which is the same as the that of y direction. The accuracy is tested up to the output time $t = 10$, namely one period of propagation. The L_1 and L_∞ errors of FDGKS-W5 and FD-W5 for viscous flow with Reynolds number $Re = 10, 100$, and 1000 are shown in Tables 5–7. We can see that FDGKS-W5 achieves very well the designed order with slightly better accuracy than those of FD-W5.

In terms of time efficiency, both inviscid (solves Euler equation) and viscous (solves Navier Stokes equation at $Re = 1000$) isotropic vertex convection problem are run on a grid of 129×129 points up to one period of time, i.e., $t = 10$. The comparison of the CPU time cost for different schemes on the same machine is shown in Table 8. For solving Euler equation, the speedup ration of FDGKS-W5 to FD-W5 is 1.92, which is lower than 2.33 for one-dimension case. It is because that the solving of two-dimension flux by GKS formula involves in the evaluation of cross derivative like a_{xy}, which is not encompassed in FD flux calculation. When Navier–Stokes equation is solved, the speedup ration of FDGKS-W5 to FD-W5 deceases to 1.39. The calculation of viscous flux by GKS approach needs to compute the one order higher moments like $\langle u^2 a_x\rangle$, $\langle u^2 a_t\rangle$, $\cdots$, shown in (24) and (26), which increases significantly the CPU time.

Example 4.6. Shock-vortex interaction

The shock-vortex interaction problem [2] is studied in a computational domain $(x, y) \in [0, 2] \times [0, 1]$. A stationary shock front is positioned at $x = 0.5$. The left upstream state is $(\rho, U, V, p) = (M^2, \sqrt{\gamma}, 0, 1)$, where γ is the specific heat ratio and $M = 1.1$ is the Mach number. A small vortex is obtained through a perturbation of the mean flow with the velocity (U, V), temperature

Table 5
Two dimensional Navier–Stokes equation with $Re = 10$; convection of viscous isotropic vortex; periodic boundary conditions. Compare the error convergence of FD-W5 and FDGKS-W5.

	FDGKS-W5				FD-W5			
$N_x \times N_y$	L_1 error	Order	L_∞ error	Order	L_1 error	Order	L_∞ error	Order
8 × 8	4.603e−3	–	2.698e−2	–	4.732e−3	–	2.612e−2	–
16 × 16	1.227e−3	1.91	7.852e−3	1.78	1.276e−3	1.89	7.568e−3	1.79
32 × 32	7.816e−5	3.97	4.645e−4	4.08	8.166e−5	3.97	4.416e−4	4.10
64 × 64	2.606e−6	4.92	1.963e−5	4.56	2.844e−6	4.86	1.538e−5	4.84
128 × 128	5.297e−8	5.64	3.243e−7	5.92	5.559e−8	5.70	3.214e−7	5.58

Table 6
Two dimensional Navier–Stokes equation with $Re = 100$; convection of isotropic vortex; periodic boundary conditions. Compare the error convergence of FD-W5 and FDGKS-W5.

	FDGKS-W5				FD-W5			
$N_x \times N_y$	L_1 error	Order	L_∞ error	Order	L_1 error	Order	L_∞ error	Order
8×8	1.910e−2	–	3.083e−1	–	1.923e−2	–	3.126e−1	–
16×16	1.091e−2	0.81	2.118e−1	0.54	1.099e−2	0.81	2.158e−1	0.53
32×32	1.222e−3	3.16	2.032e−2	3.38	1.236e−3	3.15	2.099e−2	3.36
64×64	6.324e−5	4.27	1.180e−3	4.11	6.353e−5	4.28	1.222e−3	4.10
128×128	1.671e−6	5.24	2.667e−5	5.47	1.710e−6	5.22	3.412e−5	5.16

Table 7
Two dimensional Navier–Stokes equation with $Re = 1000$; convection of isotropic vortex; periodic boundary conditions. Compare the error convergence of FD-W5 and FDGKS-W5.

	FDGKS-W5				FD-W5			
$N_x \times N_y$	L_1 error	Order	L_∞ error	Order	L_1 error	Order	L_∞ error	Order
8×8	2.355e−2	–	4.355e−1	–	2.360e−2	–	4.355e−1	–
16×16	1.476e−2	0.67	3.192e−1	0.45	1.479e−2	0.67	3.199e−1	0.45
32×32	2.128e−3	2.79	3.573e−2	3.16	2.128e−3	2.80	3.573e−2	3.16
64×64	1.435e−4	3.89	2.600e−3	3.78	1.432e−4	3.89	2.606e−3	3.78
128×128	4.634e−6	4.95	8.610e−5	4.92	4.656e−6	4.94	8.851e−5	4.88

Table 8
Inviscid and viscous vortex propagation. Mesh 129×129, CFL = 0.08, and $t = 10$. CPU time comparison of FD-W5 and FDGKS-W5.

	Euler equation			Navier–Stokes equation		
	FD-W5	FDGKS-W5	Speedup Ratio	FD-W5	FDGKS-W5	Speedup Ratio
CPU time	334.86s	174.50s	1.92	351.70s	252.64s	1.39

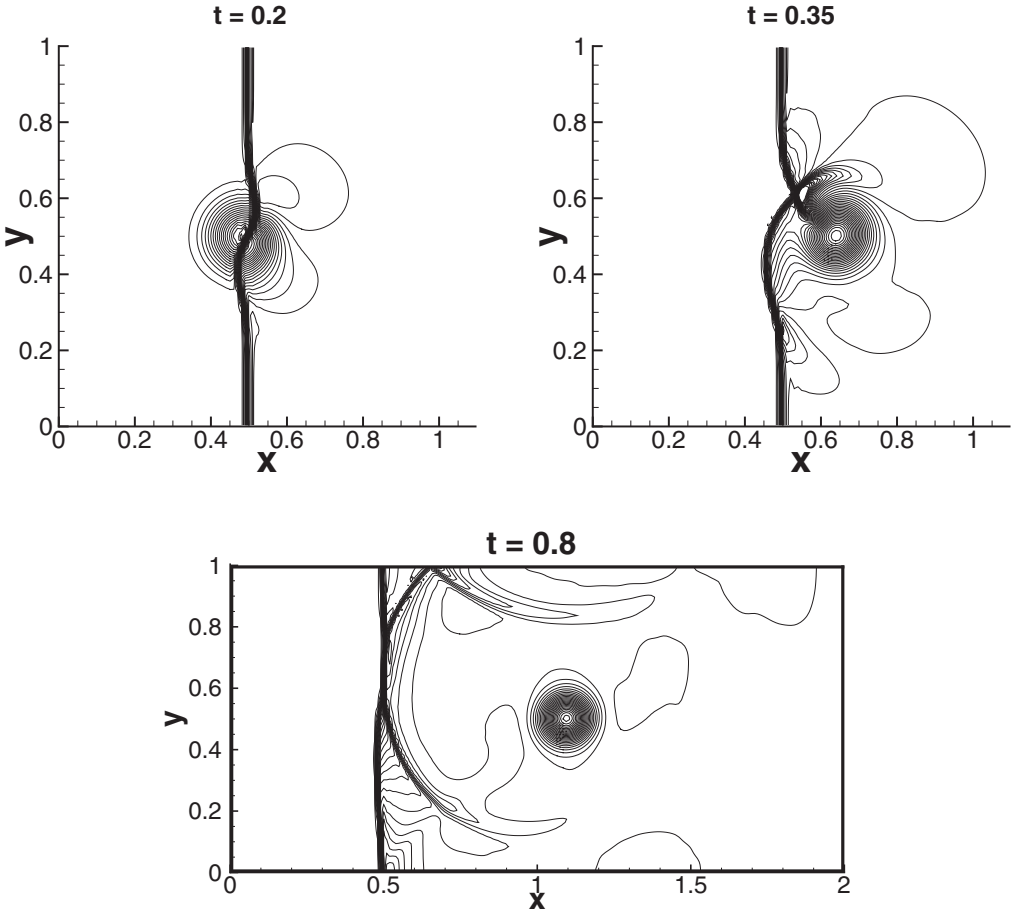

Fig. 5. Vortex shock interaction by FDGKS-W5. Grid 202×101, CFL = 0.6. Pressure contour at different time, top-left: $t = 0.2$, top-righ: $t = 0.35$, and bottom: $t = 0.8$. 60 levels between 0.8 and 1.4.

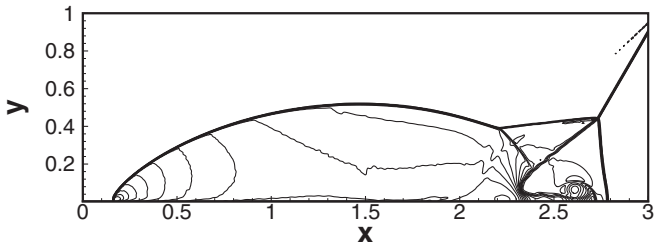

Fig. 6. Mach 10 double Mach reflection by FDGKS-W5. Number of grid 961×241, CFL = 0.6. Density contour at $t = 0.2$, 30 levels between 1.731 and 20.92.

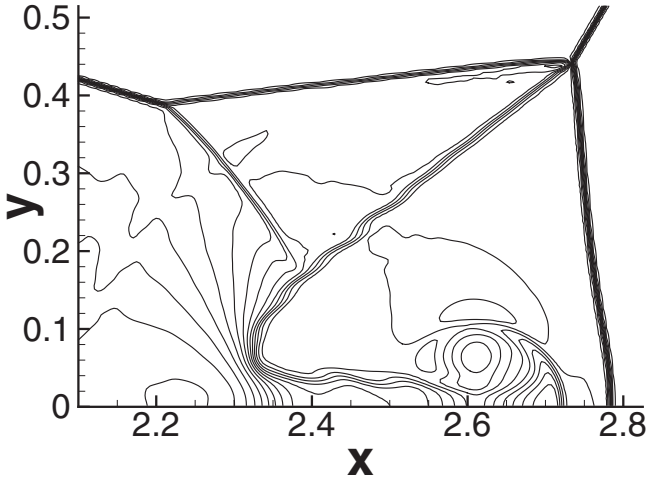

Fig. 7. Mach 10 double Mach reflection by FDGKS-W5. Zoomed in figure around triple point. Number of grid 961×241, CFL = 0.6. Density contour at $t = 0.2$, 30 levels between 1.731 and 20.92.

$(T = p/\rho)$ and entropy$(S = \ln(\frac{p}{\rho^\gamma}))$, where the perturbation is

$$\tilde{U} = \kappa\eta e^{\mu(1-\eta^2)}\sin\theta,\ \tilde{V} = -\kappa\eta e^{\mu(1-\eta^2)}\sin\theta,$$
$$\tilde{T} = -\frac{(\gamma-1)\kappa^2 e^{2\mu(1-\eta^2)}}{4\mu\gamma},\ \tilde{S} = 0, \tag{45}$$

where $\eta = r/r_c, r = \sqrt{(x-x_c)^2+(y-y_c)^2}, (x_c, y_c) = (0.25, 0.5)$ is the center of the vortex, η and μ control the strength and decay rate of the vortex, and r_c is the critical radius. Here we choose $\kappa = 0.3, r_c = 0.05$ and $\mu = 0.204$.

The gas is a diatomic molecule with $\gamma = 1.4$. The number of grid is 202×101 and CFL = 0.6. The reflected boundary condition is used on the top and bottom boundaries, and inflow and outflow boundary conditions are set on left and right boundaries, respectively. The evolution of the flow is given in Fig. 5, where both vortex and shock are well resolved.

Example 4.7. Double Mach reflection problem.

The computation domain is $[0, 4] \times [0, 1]$. A solid wall lies at the bottom of the computational domain starting from $x = 1/6$. Initially, a right-moving Mach 10 shock is positioned at $x = 1/6, y = 0$ and makes a 60° angle with the x-axis. For the bottom boundary, the exact post-shock condition is imposed for the part from $x = 0$ to $x = 1/6$ and a reflective boundary condition is used for the rest. At the top boundary of the computational domain, the flow values are set to describe the exact motion of the Mach 10 shock front. The initial pre-shock condition is

$$(\rho, p, u, v) = (8, 116.5, 8.25\cos(30^\circ), -8.25\sin(30^\circ)) \tag{46}$$

and the post-shock condition is

$$(\rho, p, u, v) = (1.4, 1, 0, 0). \tag{47}$$

The computation runs up to time $t = 0.2$. A uniform mesh with 961×241 grid points is used and CFL = 0.6. Fig. 6 shows density contours and the zoomed in figure around triple point is presented in Fig. 7. The current results agree well with that in [12].

Example 4.8. Shock-boundary layer interaction in a shock tube

This is a viscous flow problem introduced by Daru and Tenaud [3,5] to test the performance of different schemes. Daru and Tenaud and many other researchers revisited this case later, see Daru and Tenaud [4], Sjögreen and Yee [14] and coworkers. An ideal gas is at rest in a two-dimension box $0 \le x, y \le 1$. A membrane with a shock Mach number of 2.37 located at $x = 1/2$ separates two different states of the gas. At time zero, the membrane is removed and wave interaction occurs. This is a standard shock tube problem, and would give a familiar one-dimensional wave structure by solving a Riemann problem for the inviscid Euler equations. Here, the compressible Navier–Stokes equations are solved and non-slip boundary condition is implemented. The solution will develop complex two-dimensional shock/shear/boundary-layer interactions, which depend on the Reynolds number. The complex-

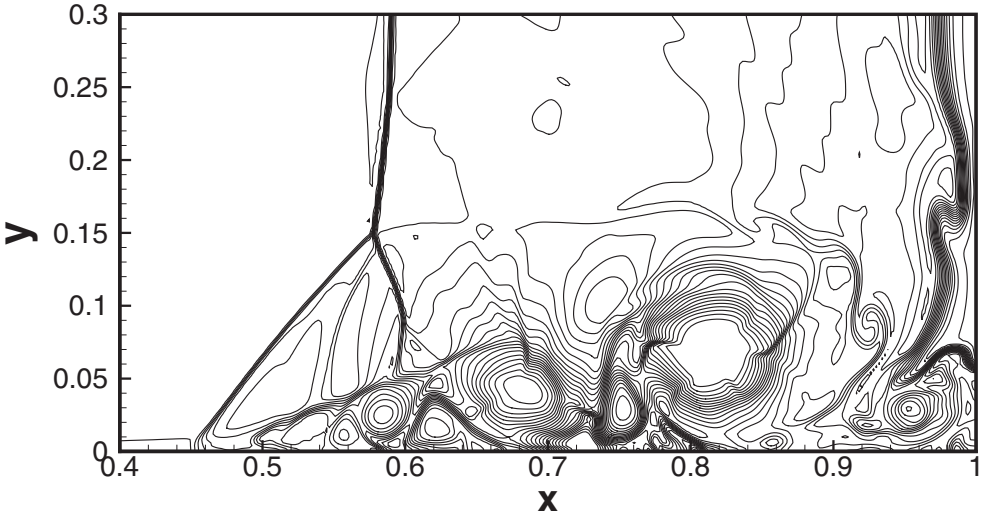

Fig. 8. Reflected shock-boundary layer interaction in a shock tube. Grid: 502×251. Contour of density, 21 contour levels between 20 and 120.

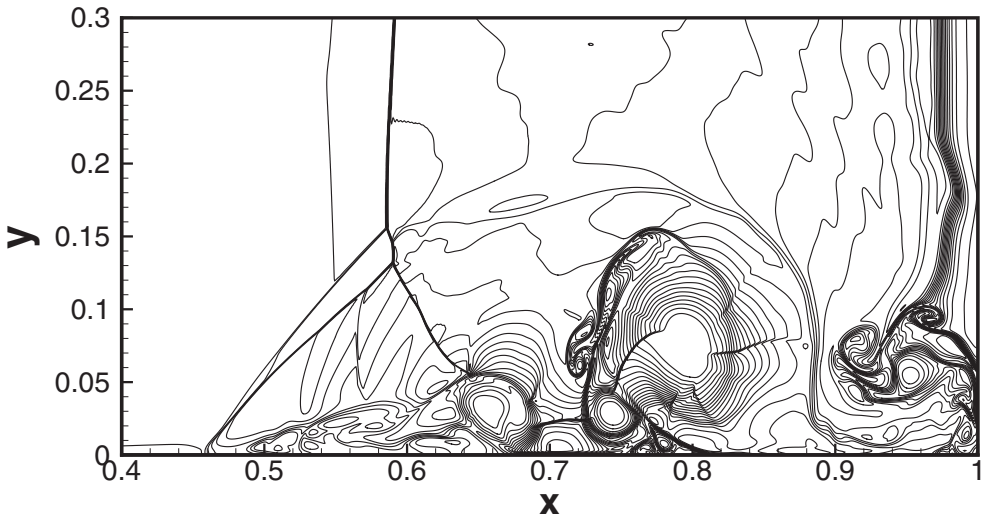

Fig. 9. Reflected shock-boundary layer interaction in a shock tube. Grid: 2002×1001. Density contour, 21 contour levels between 20 and 120.

ity of the flow structure increases with the increasing of Reynolds number.

The dimensionless initial conditions are [3],

$$\rho_L = 120,\ \ p_L = 120/\gamma,\ \ \rho_R = 1.2,\ \ p_R = 1.2/\gamma, \tag{48}$$

where ρ_L, p_L are the density and pressure, respectively, to the left of $x = 1/2$, and ρ_R, p_R to the right of $x = 1/2$. All velocities are zero initially. Diatomic gas with $\gamma = 1.4$ and the Prandtl number 0.73 are used. The Reynolds number in the current calculation is $Re = 1000$. The non-slip boundary condition and adiabatic condition for temperature on wall boundaries are imposed. The computational domain is set to be $(x, y) \in [0, 1] \times [0, 0.5]$. A symmetrical condition is used on the top boundary $x \in [0, 1], y = 0.5$.

Figs. 8 and 9 show the numerical results by FDGKS-W5 on meshes with 502×251 and 2002×1001 grid points, respectively. Compare to Daru and Tenaud's resutls [3–5], we can see that FDGKS-W5 can effectively capture the interaction of shock wave and boundary layer.

5. Conclusion

In this paper, based on time evolution of a Navier-Stokes gas distribution function and Weighted Essential Non-Oscillatory (WENO) interpolation, a high-order finite difference gas-kinetic scheme (FDGKS) is constructed. Due to the time accuracy in the gas distribution function, current FDGKS is a one-step scheme with 3rd-order in time, which has been verified by benchmark test cases. 5th-order WENO interpolation with Jiang and Shu's weight [6] has been used to capture the discontinuity. Our numerical experiments show that, with the same WENO interpolation, FDGKS presents slightly better resolution to the macroscopic equation based finite-difference method with 3rd-order TVD Runge–Kutta temporal integration (FD-RK3). As to the CPU time, compared to FD-RK3, FDGKS saves %57 in solving one-dimension Euler equation. While for the computation of two-dimensional Navier-Stokes equation, with the same central interpolation for the viscous flux, FDGKS reaches a 1.39 times of speedup compared to FD-RK3. The FDGKS is proved to be highly stable, accurate, and efficient in solving both Euler and Navier-Stokes equations. With the application of standard WENO reconstruction, it captures discontinuous solutions without oscillation. Another benefit of current FDGKS is that, compared to classical finite-difference (FD) method, it only changes the computation of pointwise flux, which makes the implementation of it to any FD code straightforward.

Acknowledgments

This work was supported by Hong Kong Research Grant Council (621709, 621011), and HKUST grants SRFI11SC05 and RPC10SC11.

References

[1] Bhatnagar PL, Gross EP, Krook M. A model for collision processes in gases I: small amplitude processes in charged and neutral one-component systems. Phys Rev 1954;94:511–25.
[2] Casper J. Finite-volume implementation of high-order essentially non-oscillatory schemes in two dimensions. AIAA J 1992;30:2829–35.
[3] Daru V, Tenaud C. Evaluation of TVD high resolution schemes for unsteady viscous shocked flows.. Comput Fluids 2001;30:89–113.
[4] Daru V, Tenaud C. High order one-step monotonicity-preserving schemes for unsteady compressible flow calculations. J Comput Phys 2004;193:563–94.
[5] Daru V, Tenaud C. Numerical simulation of the viscous shock tube problem by using a high resolution monotonicity-preserving scheme. Comput Fluids 2009;38:664–76.
[6] Jiang GS, Shu CW. Efficient implementation of weighted ENO schemes. J Comput Phys 1996;126:202–28.
[7] Li JQ, Li QB, Xu K. Comparison of the generalized Riemann solver and the gas-kinetic scheme for inviscid compressible flow simulations. J Comput Phys 2011;230:5080–99.
[8] Liu XD, Osher S. Weighted essentially non-oscillatory schemes. J Comput Phys 1994;115:200–12.
[9] Li QB, Xu K, Fu S. A high-order gas-kinetic Navier-Stokes solver. J Comput Phys 2010;229:6715–31.
[10] Luo J. A high-order Navier-Stokes flow solver and gravitational system modeling based on gas-kinetic equation. Phd thesis. Hong Kong University of Science and Technology; 2012.
[11] Ohwada T, Fukata S. Simple derivation of high-resolution schemes for compressible flows by kinetic approach. J Comput Phys 2006;211:424.
[12] Qiu J, Shu C-W. Finite difference WENO schemes with Lax-Wendroff type time discretizations. SIAM J Scient Comput 2003;24:2185–98.
[13] Shu CW, Osher S. Efficient implementation of essentially nonoscillatory shock--capturing schemes II. J Comput Phys 1989;83:32–78.
[14] Sjögreen B, Yee HC. Grid convergence of high order methods for multiscale complex unsteady viscous compressible flows. J Comput Phys 2003;185:1–26.
[15] Woodward P, Colella P. Numerical simulations of two-dimensional fluid flow with strong shocks. J Comput Phys 1984;54:115–73.
[16] Xu K. Gas-kinetic schemes for unsteady compressible flow simulations. Report 1998-03. Von Karman Institute; 1998.
[17] Xu K. A gas-kinetic BGK scheme for the navier-stokes equations, and its connection with artificial dissipation and godunov method. J Comput Phys 2001;171:289–335.
[18] Xu K, Mao ML, Tang L. A multidimensional gas-kinetic BGK scheme for hypersonic viscous flow. J Comput Phys 2005;203:405–21.
[19] Xuan LJ, Xu K. A new gas-kinetic scheme based on analytical solutions of the BGK equation. J Comput Phys 2013;234:524–39.